NASA/TM-20210020388

# Melting and Crystallization Behavior of $CaO$-$MgO$-$Al_2O_3$-$SiO_2$ Silicates Relevant to Turbine Engine Applications

*Jamesa L. Stokes and Bryan J. Harder*
*Glenn Research Center, Cleveland, Ohio*

*Valerie L. Wiesner*
*Langley Research Center, Hampton, Virginia*

*Douglas E. Wolfe*
*The Pennsylvania State University, University Park, Pennsylvania*

December 2021

# NASA STI Program . . . in Profile

Since its founding, NASA has been dedicated to the advancement of aeronautics and space science. The NASA Scientific and Technical Information (STI) Program plays a key part in helping NASA maintain this important role.

The NASA STI Program operates under the auspices of the Agency Chief Information Officer. It collects, organizes, provides for archiving, and disseminates NASA's STI. The NASA STI Program provides access to the NASA Technical Report Server—Registered (NTRS Reg) and NASA Technical Report Server—Public (NTRS) thus providing one of the largest collections of aeronautical and space science STI in the world. Results are published in both non-NASA channels and by NASA in the NASA STI Report Series, which includes the following report types:

- TECHNICAL PUBLICATION. Reports of completed research or a major significant phase of research that present the results of NASA programs and include extensive data or theoretical analysis. Includes compilations of significant scientific and technical data and information deemed to be of continuing reference value. NASA counter-part of peer-reviewed formal professional papers, but has less stringent limitations on manuscript length and extent of graphic presentations.

- TECHNICAL MEMORANDUM. Scientific and technical findings that are preliminary or of specialized interest, e.g., "quick-release" reports, working papers, and bibliographies that contain minimal annotation. Does not contain extensive analysis.

- CONTRACTOR REPORT. Scientific and technical findings by NASA-sponsored contractors and grantees.

- CONFERENCE PUBLICATION. Collected papers from scientific and technical conferences, symposia, seminars, or other meetings sponsored or co-sponsored by NASA.

- SPECIAL PUBLICATION. Scientific, technical, or historical information from NASA programs, projects, and missions, often concerned with subjects having substantial public interest.

- TECHNICAL TRANSLATION. English-language translations of foreign scientific and technical material pertinent to NASA's mission.

For more information about the NASA STI program, see the following:

- Access the NASA STI program home page at http://www.sti.nasa.gov

- E-mail your question to help@sti.nasa.gov

- Fax your question to the NASA STI Information Desk at 757-864-6500

- Telephone the NASA STI Information Desk at 757-864-9658

- Write to:
  NASA STI Program
  Mail Stop 148
  NASA Langley Research Center
  Hampton, VA 23681-2199

NASA/TM-20210020388

# Melting and Crystallization Behavior of $CaO$-$MgO$-$Al_2O_3$-$SiO_2$ Silicates Relevant to Turbine Engine Applications

*Jamesa L. Stokes and Bryan J. Harder*
*Glenn Research Center, Cleveland, Ohio*

*Valerie L. Wiesner*
*Langley Research Center, Hampton, Virginia*

*Douglas E. Wolfe*
*The Pennsylvania State University, University Park, Pennsylvania*

National Aeronautics and
Space Administration

Glenn Research Center
Cleveland, Ohio 44135

December 2021

## Acknowledgments

This work was supported by the Transformational Tools and Technologies (TTT) Project
under the NASA Transformative Aeronautics Concept Program.

This work was sponsored by the
Transformative Aeronautics Concepts Program.

*Level of Review*: This material has been technically reviewed by technical management.

Available from

NASA STI Program
Mail Stop 148
NASA Langley Research Center
Hampton, VA 23681-2199

National Technical Information Service
5285 Port Royal Road
Springfield, VA 22161
703-605-6000

This report is available in electronic form at http://www.sti.nasa.gov/ and http://ntrs.nasa.gov/

# Melting and Crystallization Behavior of $CaO\text{-}MgO\text{-}Al_2O_3\text{-}SiO_2$ Silicates Relevant to Turbine Engine Applications

Jamesa L. Stokes and Bryan J. Harder
National Aeronautics and Space Administration
Glenn Research Center
Cleveland, Ohio 44135

Valerie L. Wiesner
National Aeronautics and Space Administration
Langley Research Center
Hampton, Virginia 23666

Douglas E. Wolfe
The Pennsylvania State University
University Park, Pennsylvania 16802

## Summary

The melting and crystallization behavior of four quaternary $CaO\text{-}MgO\text{-}Al_2O_3\text{-}SiO_2$ or calcium-magnesium-aluminosilicates (CMASs) was investigated. The $CaO:SiO_2$ ratios of these systems were based on various terrestrial sources of ingested particles relevant to gas turbine engine operating environments. Melting behavior was characterized using differential scanning calorimetry, and high-temperature intrinsic crystallization products were determined by furnace heat treatments of the glasses at 1,200, 1,300, and 1,400 °C. The silicates exhibited a wide range of melting temperatures from ~1,240 up to ~1,500 °C, with most of the compositions exhibiting incongruent melting behavior. High-temperature crystallization products included $CaSiO_3$, $CaAl_2Si_2O_8$, $Ca_2MgSi_2O_7$, and $Ca(Mg,Al)Si_2O_6$, although $SiO_2$ was the only crystalline phase observed at 1,400 °C.

## 1.0 Introduction

The incorporation of ceramic matrix composites (CMCs) coated with environmental barrier coating (EBC) in gas turbine engines has aided in increasing operating temperatures and improving engine efficiency and performance (Refs. 1 and 2). However, the rise in inlet temperatures has introduced new challenges in engine materials development. A prominent issue facing EBC materials is interactions with silicate particulates primarily composed of calcium-magnesium-aluminosilicates (CMASs) and other oxides. Early studies of siliceous particulate interactions in gas turbine engines were largely focused on the mechanical damage mechanism in which silicate particulates eroded engine materials and clogged component cooling channels, which reduced engine performance (Ref. 3). However, with the rise in turbine inlet temperatures above the melting temperature of the particulate material (≥1,200 °C) and/or reduction in cooling air, CMAS damage shifts from solely mechanical to a combined mechanical and thermochemical degradation mechanism.

The thermochemical degradation of EBCs caused by CMAS is heavily dependent on particulate composition, although the composition of CMAS can vary greatly based on origin. The earliest studies of particle ingestion investigated damage to engines operating in the Middle East, including the study of Blackhawk helicopter engines operating in the Persian Gulf (Refs. 3 and 4). Engine deposits from these regions of the world were typically high in CaO content, with moderate additions of $Al_2O_3$, MgO, or FeO. NiO and $TiO_2$ were found in trace amounts, which likely come from the engine components themselves, and alkali salts such as $Na_2O$ and $K_2O$ were also found in trace amounts in these deposits. Conversely, unlike many sand-type compositions, volcanic ash is very high in $SiO_2$ content with less contribution of modifiers such as CaO, as observed in early investigations of CMAS damage of engine components from Mt. St. Helen's ash (Ref. 5). There was renewed interest in volcanic ash deposits following the 2010 Eyjafjallajökull and 2011 Grimsvötn eruptions in Iceland and the immense impact that these natural events had on airspace corridors (Refs. 6 and 7). The variation in deposit origin and composition is significant because modifiers such as CaO are extremely relevant in the crystallization of phases from the melt as a pathway for CMAS mitigation (particularly the rare-earth (RE) apatite-type silicate $Ca_2RE_8(SiO_4)O_2$ reported in several investigations (Refs. 8 to 13)).

In recent studies, prospective EBC materials were evaluated for their reaction with CMAS compositions formulated with the goal of determining thermochemical effects based on changing $CaO:SiO_2$ ratios in the glasses (Refs. 14 and 15). Besides apatite and other extrinsic crystallization products forming from the melt as a function of $CaO:SiO_2$ ratio, the changes in glass composition also influenced reaction efficacy with the EBC materials due to partial melting and some observed crystallization of the glasses themselves. Establishing the melting and crystallization products and the kinetics of the reaction pathway is important in knowing the direction the melt composition will trend. Therefore, when studying the reactivity of EBC materials with CMAS, the full evolution of the melt needs to be considered. Preliminary CMAS property data was briefly reported in these investigations (Ref. 14), but full analysis and findings of the CMAS compositions have not yet been reported in literature. Assessment of the glass composition thermal properties must be carried out to better understand the behavior of these glasses with coating materials. Thus, the purpose of this study is to report melting and crystallization properties of synthetic CMAS compositions formulated with varying $CaO:SiO_2$ ratios used in molten silicate reactivity testing with EBC and thermal barrier coating (TBC) materials.

# 2.0 Experimental Methods

## 2.1 Glass Formulation

Four CMAS compositions were formulated based on relevancy to previous studies and the turbine engine operating environment. The Krämer (Ref. 16) glass was used in many investigations of coating materials with CMAS and was originally formulated based on early studies of siliceous deposits in gas turbine engines (Ref. 4). The focus of many investigations on a single CMAS composition readily allows for direct comparison of corrosion behavior between studies, but such a methodology is limited in the scope of understanding the transitions between degradation mechanisms. $CaO:SiO_2$ ratios of two additional CMAS compositions were determined from a desert sand composition previously investigated for its thermal and mechanical properties (Ref. 17) and chemical analysis on 2010 Eyjafjallajökull volcanic ash (Table 1).

As shown in Table 1, glassy deposits in turbine engines are typically multicomponent, complex systems that also have alkali oxides such as $Na_2O$ and $K_2O$, as well as iron oxides. In this study, the melting and crystallization of glasses as a function of $CaO:SiO_2$ are being evaluated. Thus, the model CMAS compositions mentioned previously were normalized into calcia-magnesia-alumina-silica systems. Degradation mechanisms are generally controlled by CaO and $SiO_2$ content, so these systems have been simplified to four-component systems to study the effects of this ratio (Table 2). This was done by a weighted division of the other oxide content based on the existing individual amounts of CaO, MgO, $Al_2O_3$, and $SiO_2$. By normalizing the compositions in this way, the $CaO:SiO_2$ ratio is kept equal to the original composition. An example of this normalization is shown in Equation (1) for CaO:

$$\mathrm{CaO}_n = \mathrm{CaO}_o + \left( \frac{\mathrm{CaO}_o}{\mathrm{CaO}_o + \mathrm{MgO}_o + \mathrm{Al_2O_3}_o + \mathrm{SiO_2}_o} \cdot X \right) \tag{1}$$

The *n* subscript represents the normalized mole percent of the oxide and the *o* subscript represents the original mole percent of the oxide. *X* is the total mole percent of the other oxides present in the glass.

TABLE 1.—REFERENCE DEPOSIT COMPOSITIONS

| Oxide, mol% | Krämer (Ref. 16) | Desert sand (Ref. 17) | Eyjafjallajökull volcanic ash |
|---|---|---|---|
| CaO | 35.00 | 27.8 | 6.15 |
| MgO | 10.00 | 4.0 | 4.18 |
| $Al_2O_3$ | 7.00 | 5.0 | 10.02 |
| $SiO_2$ | 48.00 | 61.6 | 66.99 |
| $Fe_2O_3$ | --------- | 0.6 | 4.41 |
| $K_2O$ | --------- | 1.0 | 1.21 |
| $Na_2O$ | --------- | -------- | 5.00 |
| $TiO_2$ | --------- | -------- | 1.39 |
| Trace | --------- | <0.5 | 0.66 |
| $CaO:SiO_2$ | 0.729 | 0.451 | 0.092 |

TABLE 2.—REFERENCE DEPOSIT COMPOSITIONS, NORMALIZED TO FOUR-COMPONENT SYSTEMS

| Oxide, mol% | Krämer (Ref. 16) | Desert sand (Ref. 17) | Eyjafjallajökull volcanic ash |
|---|---|---|---|
| CaO | 35.00 | 28.25 | 7.04 |
| MgO | 10.00 | 4.07 | 4.79 |
| $Al_2O_3$ | 7.00 | 5.08 | 11.47 |
| $SiO_2$ | 48.00 | 62.60 | 76.70 |
| $CaO:SiO_2$ | 0.729 | 0.451 | 0.092 |

Additionally, the $MgO\text{-}Al_2O_3$ molar content was kept constant between the compositions and equal to the Krämer glass so that only behavior based on differences in CaO and $SiO_2$ content were observed here. This was done by setting up a system of equations based on the compositions of the reference CMAS glasses. The $CaO:SiO_2$ ratios of these glasses are constant $c$, expressed as

$$c = \frac{x}{y} \tag{2}$$

where $x$ is the mole percent of CaO and $y$ is the mole percent of $SiO_2$. The sum of $x$ and $y$ is equal to the total (100) minus the remaining oxides $z$ as

$$x + y = 100 - z \tag{3}$$

where $z$ is the total sum of $(MgO+Al_2O_3)$. Using these two equations, $SiO_2$ ($y$) for each composition was calculated as

$$y = \frac{100 - z}{1 + c} \tag{4}$$

and CaO ($x$) as

$$x = 100 - z - y \tag{5}$$

These nominal compositions are renamed CMAS–1 (Krämer), CMAS–2 (desert sand), and CMAS–3 (Eyjafjallajökull volcanic ash) in this study and are listed in Table 3. Given the large gap in $CaO:SiO_2$ ratio between CMAS–2 and CMAS–3, an additional CMAS glass (CMAS–2.5) was developed as a midpoint $CaO:SiO_2$ ratio composition between CMAS–2 and CMAS–3.

TABLE 3.—NOMINAL COMPOSITIONS OF CALCIUM-MAGNESIUM-ALUMINOSILICATE (CMAS) GLASSES

| Oxide, mol% | CMAS–1 | CMAS–2 | CMAS–2.5 | CMAS–3 |
|---|---|---|---|---|
| CaO | 35.000 | 25.810 | 17.723 | 6.975 |
| MgO | 10.000 | 10.000 | 10.000 | 10.000 |
| $Al_2O_3$ | 7.000 | 7.000 | 7.000 | 7.000 |
| $SiO_2$ | 48.000 | 57.190 | 65.277 | 76.025 |
| $CaO:SiO_2$ | 0.729 | 0.451 | 0.271 | 0.092 |

TABLE 4.—COMPOSITIONS OF SYNTHESIZED CALCIUM-MAGNESIUM-ALUMINOSILICATE (CMAS) GLASSES, DETERMINED BY INDUCTIVELY COUPLED PLASMA ATOMIC EMISSION SPECTROSCOPY

| Oxide, mol% | CMAS–1 | CMAS–2 | CMAS–2.5 | CMAS–3 |
|---|---|---|---|---|
| CaO | 32.766 | 26.720 | 17.768 | 7.259 |
| MgO | 8.820 | 9.778 | 10.218 | 9.568 |
| $Al_2O_3$ | 6.843 | 7.665 | 7.859 | 7.660 |
| $SiO_2$ | 51.571 | 55.836 | 64.155 | 75.512 |
| $CaO:SiO_2$ | 0.635 | 0.479 | 0.277 | 0.096 |

### 2.2 Calcium-Magnesium-Aluminosilicate (CMAS) Glass Synthesis

$CaCO_3$ (>99.0 percent from Alfa Aesar), MgO (99.95 percent from Cerac, Inc.), $Al_2O_3$ (>99.0 percent from Almatis, Inc.), and $SiO_2$ (99.5 percent from Alfa Aesar) were used as starting powders for glass synthesis. The powders were mixed in their respective weight ratios in ethanol using 10-mm spherical $Al_2O_3$ media on a ball mill for 24 h. The mixtures were dried on a hotplate before heat treatment in a box furnace. The furnace was ramped 1 °C/min to 850 °C, holding for 10 h to burn off $CO_2$ and prevent boilover during melting. The heat-treated powders were then placed in a platinum crucible and melted in a box furnace at 1,500 °C with a ramp rate of 10 °C/min. After a 1-h hold, the melt was quenched in water to produce a glass. The resulting glass frit was ground in a mortar and pestle before milling again in ethanol using 10-mm spherical $Al_2O_3$ media for 24 h to obtain fine glass powders. The compositions of the final glass powders were determined using inductively coupled plasma atomic emission spectroscopy and are listed in Table 4.

### 2.3 Furnace Heat Treatments and Characterization

The glass powders were uniaxially pressed into ~1-g pellets with a diameter of 12.7 mm and heat treated in a box furnace in platinum foil crucibles. The pellets were heated at a ramp rate of 10 °C/min to 1,200, 1,300, and 1,400 °C with an isothermal hold at 1 h, followed by quenching in air using a cooling fan. Measurement of sample temperature after furnace removal resulted in estimated quench rates of ~900 to 1,000 °C/min. The samples were then cross sectioned. One half of a cross-sectioned pellet was polished to a 1-μm finish using conventional metallographic techniques, and the other half was crushed and ground into a powder in a mortar and pestle.

Differential scanning calorimetry (DSC) was carried out to determine crystallization and melting temperatures of the synthesized glasses. The experiments were performed in air on a Netzsch STA 409 instrument using platinum crucibles with lids. The platinum crucibles were placed on sapphire ($Al_2O_3$) to prevent adhesion to the sample stage during analysis. Samples were measured from room temperature to 1,500 °C at a ramp rate of 10 °C/min under airflow of 50 mL/min. An empty crucible was heated with the program to obtain a temperature calibration curve, and a sapphire standard was run to obtain a baseline curve for measurement. Finally, sample powders were weighed out between ~20 to 30 mg so that the mass of the sample was similar to the mass of the standard. Sample powders were placed into the platinum crucibles and pressed into compacts before analysis. Each sample was run on one cycle of the described temperature program.

Crystallographic information was obtained on the as-synthesized and heat-treated CMAS using x-ray diffraction (XRD) (D8 Advance, Bruker). XRD results were analyzed using whole pattern fitting to determine relative amounts of crystalline phases with JADE software (Materials Data, Inc.). Microstructural features of the polished pellet cross sections were characterized by scanning electron microscopy (SEM) (Thermo Fisher (FEI Company) Q250 Environmental SEM, Phenom ProX). Compositional analysis was carried out using energy dispersive spectroscopy (EDS) and was used to confirm crystalline reaction products observed in XRD.

## 3.0 Results

### 3.1 Calcium-Magnesium-Aluminosilicate (CMAS) Melting Temperature and Behavior

The XRD analysis of the as-synthesized glasses is displayed in Figure 1. There are noticeable amorphous humps in all the scans and no peak indicating detectable crystallinity. The amorphous humps

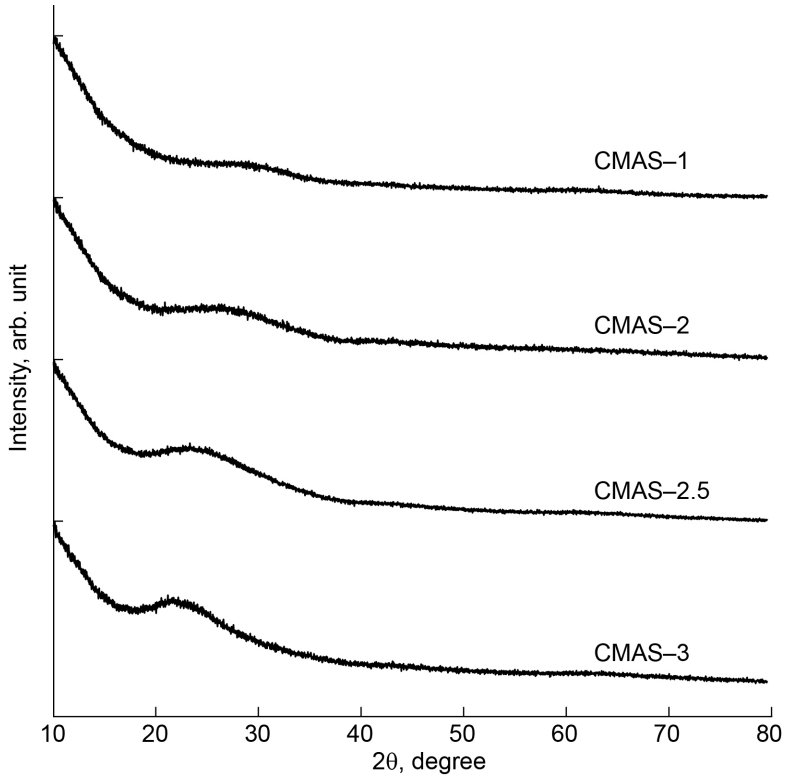


Figure 1.—X-ray diffraction scans of starting calcium-magnesium-aluminosilicate (CMAS) glasses. Diffraction angle (θ).

exhibit shifts to lower angles and increases in intensity as $SiO_2$ content in the glass increases. Figure 2 shows the DSC graphs of the CMAS glasses tested up to 1,500 °C. The change in heat was measured in watts (W, joules per second) per gram. The DSC scan of CMAS–1 is displayed in Figure 2(a) and shows peaks indicating both crystallization and melting events occurring during evaluation. The two exothermic peaks between 950 to 1,050 °C indicated crystallization of the glass occurring within this range of temperature, while the very sharp endothermic peak between ~1,210 to 1,260 °C was indicative of melting. The sharp nature of this endothermic peak suggests congruent melting of the glass within this temperature range, which may be characteristic of a eutectic composition.

Like CMAS–1, DSC results of CMAS–2 (Figure 2(b)) also indicated crystallization of the glass occurring in the range of ~950 to 1,050 °C, although the melting behavior was more complex than that of CMAS–1. The endothermic peak in the CMAS–2 scan began at ~1,150 °C. However, the three overlapping endothermic peaks in the DSC data may suggest that melting of this composition occurred in three steps, with the completion of melting at ~1,290 °C. The exothermic peaks corresponding to crystallization events for CMAS–2.5 were shifted to slightly higher temperatures than CMAS–2 at ~1,000 to 1,175 °C. Compared to CMAS–2, melting of CMAS–2.5 (Figure 2(c)) occurred in a much narrower range of temperatures. The shape of the endothermic peak was very sharp, similar to the eutectic nature of CMAS–1, although there were slight shoulders on both sides of this peak. In CMAS–3 (Figure 2(d)), crystallization and melting of the glass occurred in a much smaller range of temperatures, between ~1,190 and ~1,250 °C. Unlike CMAS–1 and CMAS–2, the exothermic behavior of CMAS–3 was exhibited by a much smaller peak in magnitude, followed by a very sharp endothermic peak, possibly indicating some eutectic melting behavior of part or all of the glass composition. In all the scans, no other exothermic peaks were observed after melting events, likely demonstrating that additional crystallization is no longer favorable above the melting temperatures identified in the DSC scans.

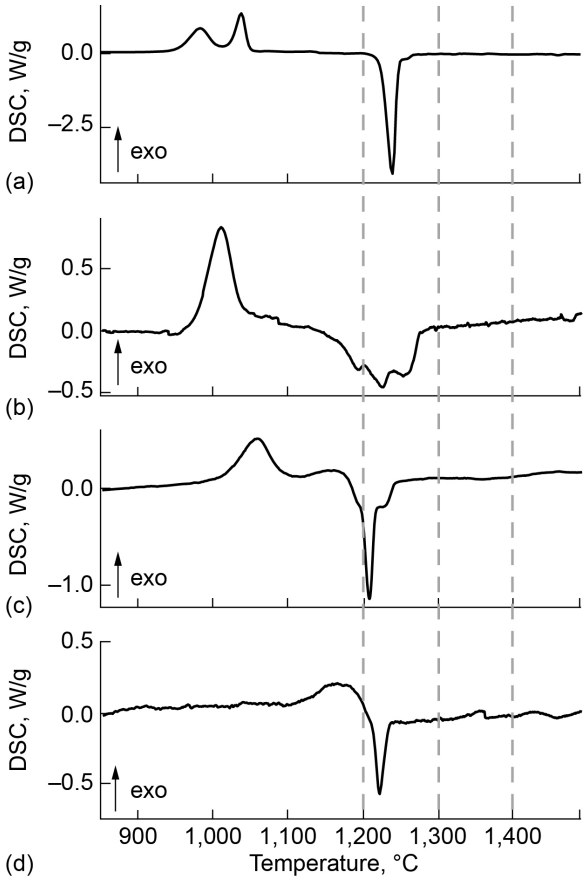


Figure 2.—Differential scanning calorimetry (DSC) scans at 10 °C/min of calcium-magnesium-aluminosilicate (CMAS). (a) CMAS–1. (b) CMAS–2. (c) CMAS–2.5. (d) CMAS–3. Dashed lines indicate temperatures utilized for furnace heat treatments. Y-axes in graphs are not shared and vary in magnitude.

Because DSC baseline and standard measurements were made prior to running scans on the glass powders, it was possible to quantify the evolution of heat during crystallization and melting. Using code written in Python programming language (Python Software Foundation), the areas of the exothermic and endothermic peaks in the DSC data were estimated. The area under the DSC curve is equal to the total amount of heat exchanged during the reaction, which at constant pressure, is equal to the change in enthalpy $H$ (Ref. 18). The DSC curves are plots of the change in heat $Q$ measured over the change in temperature $T$, as

$$\Delta Q = \frac{\partial Q}{\partial T} \tag{6}$$

The temperature of the sample is related to the heating rate β (change in $T$ over time $t$) during analysis,

$$\beta = \frac{\mathrm{d}T}{\mathrm{d}t} \tag{7}$$

and the change in $Q$ over $t$ is calculated as

$$\frac{\partial Q}{\partial T} \cdot \frac{\mathrm{d}T}{\mathrm{d}t} = \frac{\partial Q}{\partial t} \tag{8}$$

The change in $H$ is then equal to the integral of the change in $Q$ over $t$ as

$$\Delta H = \int_0^t \frac{\partial Q}{\partial t} \mathrm{d}t \tag{9}$$

Thus, for the exothermic peaks, the $H$ of crystallization was calculated, and the $H$ (or heat) of fusion was calculated for the endothermic peaks. Gaussian distributions were fitted onto the DSC data as the approximate functions for the peaks, with the sum of the peaks as an approximation of the entire DSC curve:

$$f\left(t, \mu_n, \sigma_n, A_n\right) = \sum_1^n A_n \exp\left(-\frac{\left(t-\mu_n\right)^2}{2\sigma_n^2}\right) \tag{10}$$

where μ is the mean, σ is the standard deviation, and $A$ is the amplitude of each distribution. Figure 3 displays the graphs of the Python analysis, and the calculated enthalpies from each peak for all the CMAS compositions listed in Table 5.

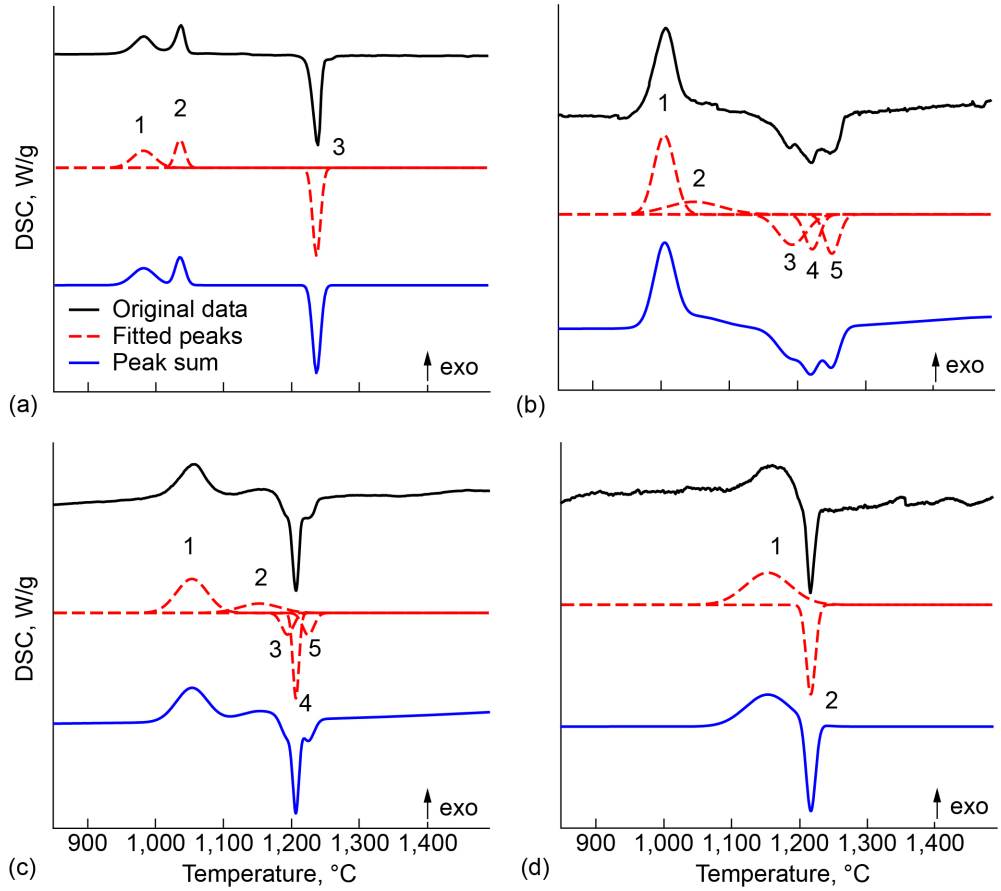


Figure 3.—Peak fitting results of differential scanning calorimetry (DSC) data of calcium-magnesium-aluminosilicate (CMAS). (a) CMAS–1. (b) CMAS–2. (c) CMAS–2.5. (d) CMAS–3. Calculated enthalpies of labeled peaks are listed in Table 5.

TABLE 5.—CALCULATED CALCIUM-MAGNESIUM-ALUMINOSILICATE (CMAS) ENTHALPIES OF CRYSTALLIZATION AND FUSION FROM PEAKS FITTED IN FIGURE 3

| Sample | Exothermic, J/g | Endothermic, J/g |
|---|---|---|
| CMAS–1 | Peak 1: 192.1<br>Peak 2: 137.8 | Peak 3: –358.4 |
| CMAS–2 | Peak 1: 190.3<br>Peak 2: 41.8 | Peak 3: –95.3<br>Peak 4: –53.3<br>Peak 5: –62.6 |
| CMAS–2.5 | Peak 1: 156.6<br>Peak 2: 52.9 | Peak 3: –36.7<br>Peak 4: –75.5<br>Peak 5: –36.7 |
| CMAS–3 | Peak 1: 93.2 | Peak 2: –43.1 |

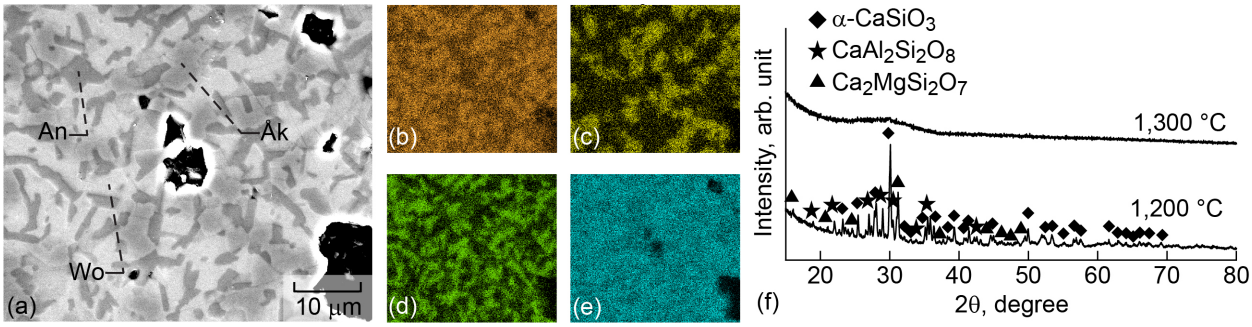


Figure 4.—Calcium-magnesium-aluminosilicate (CMAS) images. (a) Backscattered emission (BSE) micrograph of CMAS–1. Anorthite (An). Wollastonite (Wo). Åkermanite (Åk). Energy dispersive spectroscopy maps after heat treatment at 1,200 °C for 1 h. (b) Calcium. (c) Magnesium. (d) Aluminum. (e) Silicon. (f) X-ray diffraction scans of CMAS–1 after heat treatment. Diffraction angle (θ).

## 3.2 Calcium-Magnesium-Aluminosilicate (CMAS) Furnace Heat Treatments

Furnace heat treatments were performed on pressed pellets of the CMAS glasses at 1,200, 1,300, and 1,400 °C for 1 h, and the subsequent crystallization products were investigated and identified through a combination of SEM and XRD. CMAS–1 (Figure 4(a)) crystallized to wollastonite (α-$CaSiO_3$), anorthite ($CaAl_2Si_2O_8$), and åkermanite ($Ca_2MgSi_2O_7$) at 1,200 °C, while diopside ($Ca(Mg,Al)Si_2O_6$) and anorthite crystallized in CMAS–2 at this temperature (Figure 5). The high-residual amorphous content in CMAS–2 was evidenced by the large residual glass matrix surrounding the diopside (brighter phase) and anorthite precipitates in Figure 5(a). Conversely, CMAS–1 seemed to be largely crystalline at 1,200 °C, as evidenced by the backscattered emission (BSE) micrograph in Figure 4(a). Additionally, while CMAS–2 still exhibited a slight amorphous region in the XRD data, an amorphous region was not observed in CMAS–1. Both CMAS–1 and CMAS–2 became fully molten again at 1,300 °C, showing good agreement with the melting and crystallization behavior observed in the DSC analysis.

CMAS–2.5 exhibited crystallization of diopside and cristobalite ($SiO_2$) at 1,200 °C. There was cracking observed in the cristobalite phase, possibly due to the high-low polymorph phase transformation (Ref. 19). Like CMAS–2, there was a substantial residual matrix observed in SEM micrographs (Figure 6(d)) at this temperature. At both 1,300 and 1,400 °C, crystalline phases are detectable in XRD analysis, although the

peaks decreased greatly in magnitude from the intensity at 1,200 °C. This indicates a decrease in crystallinity and an increase in residual melt content at these higher temperatures (Figure 6(b) and (c)). As shown in Figure 7(a), CMAS–3 crystallized to enstatite ($MgSiO_3$), as well as anorthite and cristobalite at 1,200 °C. Like CMAS–2.5, crystalline phases were still observed at 1,300 and 1,400 °C. SEM results in Figure 7(b) (1,300 °C) and Figure 7(g) (1,400 °C) showed cristobalite present in a residual glass matrix. XRD analysis of CMAS–3 (not shown here) confirmed cristobalite as the crystalline phase of $SiO_2$, with peaks of both the high and low cristobalite polymorphs present.

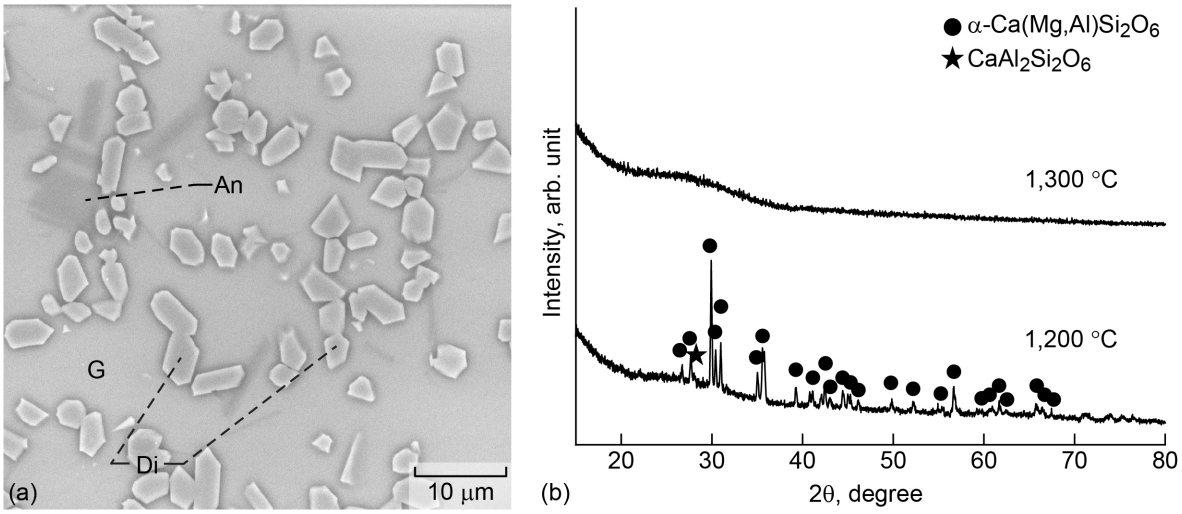


Figure 5.—Calcium-magnesium-aluminosilicate (CMAS) images. (a) Backscattered emission micrograph of CMAS–2 after heat treatment at 1,200 °C for 1 h. Anorthite (An). Diopside (Di). Glass (G). (b) X-ray diffraction scans of CMAS–1 after heat treatment. Diffraction angle (θ).

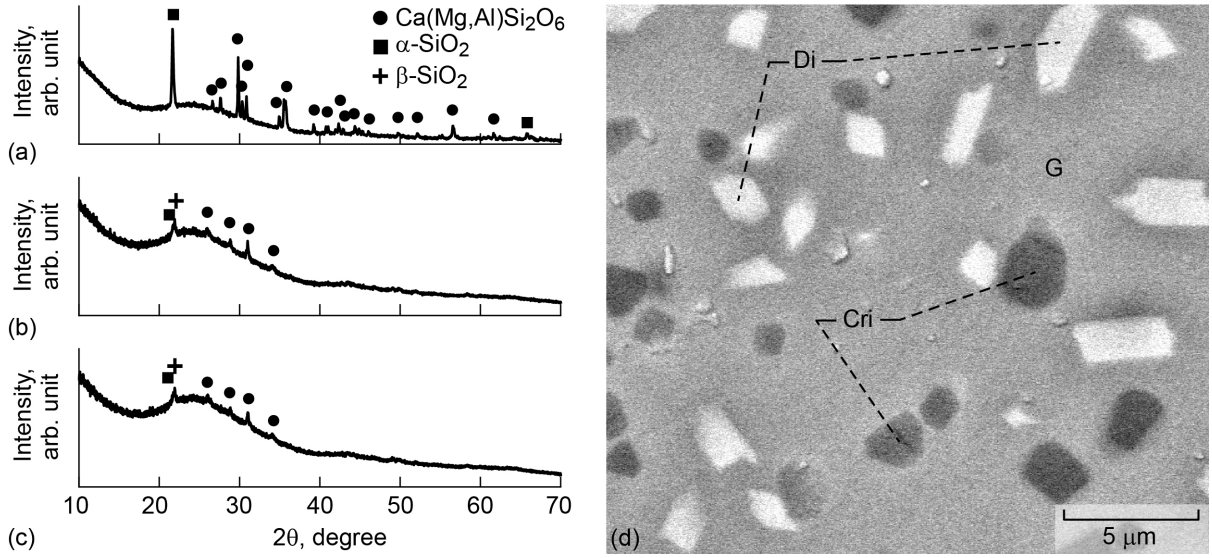


Figure 6.—X-ray diffraction scans of calcium-magnesium-aluminosilicate (CMAS–2.5) after heat treatment at (a) 1,200 °C for 1 h, (b) 1,300 °C for 1 h, and (c) 1,400 °C for 1 h. Diffraction angel (θ). (d) Backscattered emission micrograph of CMAS–2.5 after heat treatment at 1,200 °C for 1 h. Diopside (Di). Glass (G). Cristobalite (Cri).

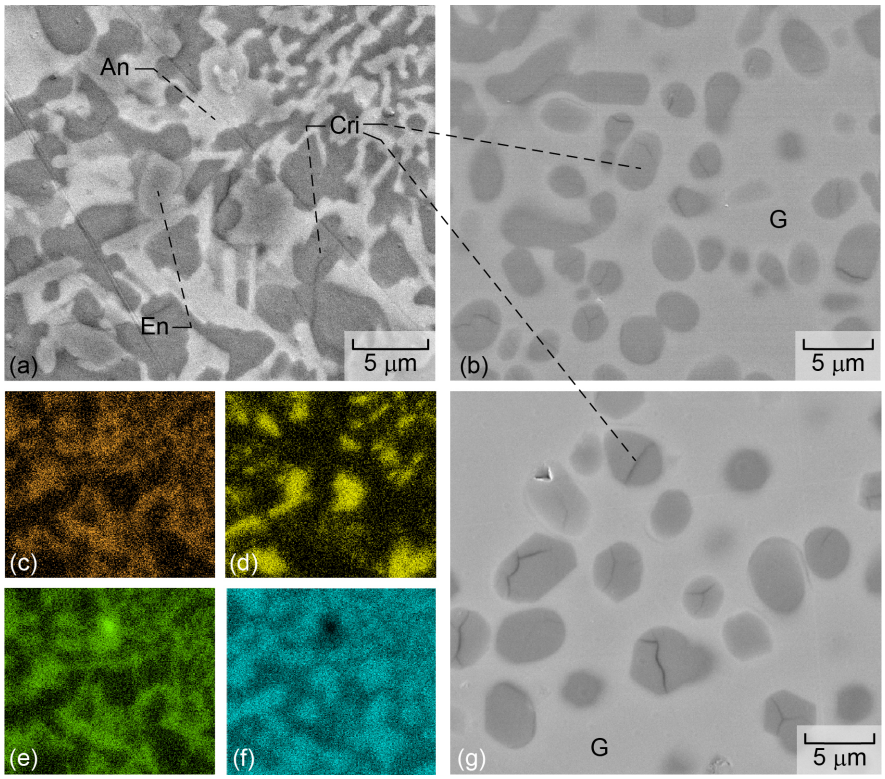


Figure 7.—Calcium-magnesium-aluminosilicate (CMAS) images. (a) Backscattered emission (BSE) micrograph. (b) BSE micrograph of CMAS–3 after heat treatment at 1,300 °C for 1 h. Energy dispersive spectroscopy maps of CMAS–3 after heat treatment at 1,200 °C for 1 h. (c) Calcium. (d) Magnesium. (e) Aluminum. (f) Silicon. (g) BSE micrograph of CMAS–3 after heat treatment at 1,400°C for 1 h. Anorthite (An). Clinoenstatite (En). Cristobalite (Cri). Glass (G).

## 4.0 Discussion

It was expected that the endpoints of melting of the compositions would shift to higher temperatures with the decrease in $CaO:SiO_2$ ratio. The endpoint of melting for CMAS–2 was ~1,290 °C, about ~20 °C higher than CMAS–1, although its onset of melting was ~60 °C lower than CMAS–1. For both CMAS–2.5 and CMAS–3, the endpoints of melting events observed in the DSC trace were ~1,240 and ~1,235 °C, respectively. However, the heat treatments at 1,300 and 1,400 °C indicated the presence of crystalline phases at these temperatures. As previously noted, these glasses were melted at 1,500 °C for 1 h to obtain completely amorphous materials, and additional melting could have occurred outside the analysis range. It is believed that all crystallization events were captured in the DSC scans of the glass. Thus, if complete melting occurred after crystallization within the range of temperatures tested, due to conservation of energy, the total measured enthalpy of crystallization should be roughly equal to the total measured enthalpy of fusion. The differences between the total enthalpies of crystallization and fusion were ~8, ~9, ~33, and ~73 percent for CMAS–1, CMAS–2, CMAS–2.5, and CMAS–3, respectively. While the fit of Equation (10) could contribute to this difference, the $R^2$ values for the four CMAS compositions were 0.9798, 0.9956, 0.9915, and 0.9757, respectively, which are representative of the quality of fit to the original DSC data. Since heat treatment studies confirmed full melting of CMAS–1 and CMAS–2 above 1,260 and 1290 °C, respectively, this ~8 to 9 percent difference between enthalpies can also be attributed to the error associated with this estimation technique, as all crystallization and melting events for CMAS–1 and CMAS–2 have occurred within the range of temperatures tested in DSC. In this case, subtracting this error from CMAS–2.5

and CMAS–3, there is still a ~24 and ~64 percent difference, respectively, between the exothermic and endothermic events observed in the DSC data. The actual values of these differences are 60.6 and 50.1 J/g, meaning that there was slightly more heat evolution for crystallization events over melting events within the temperatures tested, which supports the possibility that additional melting occurred outside the range of temperatures tested.

In addition to changes in melting behavior, the change in $CaO:SiO_2$ ratio shifts the glasses into varying phase regions in the quaternary $CaO\text{-}MgO\text{-}Al_2O_3\text{-}SiO_2$ system. Each CMAS composition studied here is plotted on the liquidus diagram in Figure 8, which is a $CaO\text{-}MgO\text{-}SiO_2$ ternary system at 15 wt% $Al_2O_3$ (the CMAS compositions were formulated at ~12 wt% $Al_2O_3$).

At similar $Al_2O_3$ content, this diagram was used for phase comparison between the CMAS compositions. CMAS–1 exhibited probable eutectic behavior in DSC analysis (Figure 2(a)), as melting occurred within a very small temperature range. The eutectic behavior is consistent with previous analyses of this CMAS composition and the location on the phase diagram in Figure 8 (Ref. 16). CMAS–1 falls within the anorthite region of the phase diagram, and from microscopic analysis, it appeared that anorthite (dark gray) crystallized first from the melt, as the wollastonite (lightest gray) and åkermanite (intermediate gray) precipitates formed an overlay over the anorthite (Figure 4(a)). Whole pattern fitting results of the XRD scans of the glasses are listed in Table 6, the values of which are pertaining to the ratios of the crystalline products in each CMAS system. After heat treatment at 1,200 °C, the amount of wollastonite and anorthite formation was roughly equal, whereas there was almost two times the amount of wollastonite over åkermanite. Because the synthesized glass composition was not exactly on the 10 mol% MgO line, it is possible that the crystallization path upon heating could have gone towards the boundary of the wollastonite-anorthite regions, which would shift away from the eutectic point, and result in a less congruent melting than what was hypothesized based on DSC analysis.

Both SEM and DSC analysis indicated incongruent melting of CMAS–2, which also falls within the anorthite region, but very close to the boundary of the pyroxene region (a solid solution range consisting of diopside and enstatite). As shown in the DSC analysis (Figure 2), this composition likely melts in three steps, becoming completely molten again at 1,300 °C (confirmed via heat treatment data). No phase other than anorthite and diopside was observed with this CMAS composition after furnace heat treatments, so it is difficult to discern whether, upon heating, the crystallization path moves toward the intersection of the anorthite-pyroxene-melilite regions or the intersection of the anorthite-pyroxene-tridymite regions. However, any additional phase that was present may crystallize at lower temperatures and then become molten again by 1,200 °C. It is possible that åkermanite (an end member of melilite) could form, but additional heat treatments are needed below 1,200 °C to confirm. At higher $SiO_2$ content, CMAS–2.5 falls almost on the point of intersection of the anorthite-pyroxene-tridymite regions, although cristobalite was the $SiO_2$ polymorph observed in heat treatments of this CMAS composition. Theoretically, tridymite forms from β-quartz upon heating above ~870 °C, then transforming to cristobalite around ~1,470 °C. However, many findings have indicated that the tridymite transformation is bypassed in favor of directly forming cristobalite in pure $SiO_2$ (Refs. 21 and 22). Cristobalite also crystallized in CMAS–3, which is within the $SiO_2$-rich region of the diagram. As cristobalite was still observed at 1,300 and 1,400 °C, the endothermic peak in the CMAS–3 DSC scans could be attributed to the congruent melting of enstatite and anorthite in this system above 1,200 °C. In these $SiO_2$-rich CMAS compositions, while it is desirable to see crystallization up to 1,400 °C, crystallization of cristobalite may not be ideal, as the phase does exhibit extensive cracking due to the high-low polymorph phase transformation, which could provide additional pathways for infiltration of the residual melt.

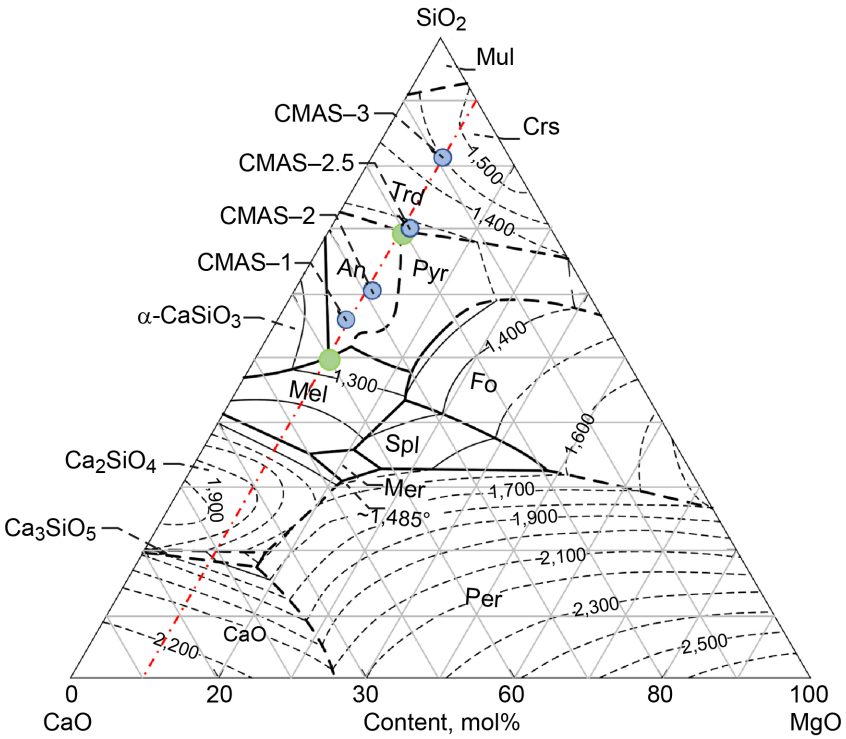


Figure 8.—CaO-MgO-$SiO_2$ liquidus diagram at 15 wt% $Al_2O_3$ (Ref. 20). Calcium-magnesium-aluminosilicate (CMAS) compositions synthesized in this study are highlighted by blue circles, and MgO content is highlighted with red line. Possible eutectic points observed in this study are highlighted by green circles. Anorthite (AN). Cristobalite (Crs). Forsterite (Fo). Melilite (Mel). Merwinite (Mer). Mullite (Mul). Periclase (Per). Pyroxene (Pyr). Spinel (Spl). Tridymite (Trd).

TABLE 6.—WHOLE PATTERN FITTING RESULTS OF RELATIVE RATIOS OF CRYSTALLINE PRODUCTS IN WEIGHT PERCENT (wt%) FORMED AFTER HEAT TREATMENT AT 1,200 °C FOR 1 h

| Sample | Wollastonite α-$CaSiO_3$ | Anorthite $CaAl_2Si_2O_8$ | Åkermanite $Ca_2MgSi_2O_7$ | Diopside $Ca(Mg,Al)Si_2O_6$ | Enstatite $MgSiO_3$ | Cristobalite $SiO_2$ |
|---|---|---|---|---|---|---|
| CMAS–1 | 42.1 | 38.3 | 19.6 | ------ | ----- | ----- |
| CMAS–2 | ----- | 12.1 | ----- | 87.9 | ----- | ----- |
| CMAS–2.5 | ----- | ----- | ----- | 58.4 | ----- | 41.6 |
| CMAS–3 | ----- | 28.4 | ----- | ----- | 28.5 | 43.1 |

$SiO_2$ crystallization was observed in two of the four CMAS compositions (CMAS–2.5 and CMAS–3), but anorthite seems to be a common phase appearing in heat treatments of not only the CMAS compositions within this study, but within other silicate systems investigated for interactions with coating materials (Refs. 23 to 27). In order to increase the CMAS resistance of 7 wt% yttria-stabilized zirconia (7YSZ), Aygun et al. investigated codoping with $Al_2O_3$ and $TiO_2$, showing that the combination of both $Al^{3+}$ and $Ti^{4+}$ provided an excess of $Al^{3+}$ for ease of anorthite ($CaAl_2Si_2O_8$) crystallization and nucleation sites with $Ti^{4+}$ (Ref. 28). Anorthite on its own melts at ~1,550 °C (Ref. 29), so it was hypothesized that this reaction could result in a barrier layer to prevent further CMAS infiltration. However, in the current study, anorthite did crystallize only as a low-temperature phase and was no longer observed above this

temperature. Additionally, it is currently unknown as to why anorthite was not observed in CMAS–2.5 heat treatments. Based on current results, crystallization of anorthite may be beneficial in CMAS mitigation at 1,200 °C and below, but additional factors such as kinetics may prevent formation of this phase in certain CMAS compositions.

From these results, a concern arises to the incongruent melting of all the CMAS glasses synthesized except for CMAS–1. Because melting does not occur at a single temperature, there is the possibility of partial reactions occurring when these glasses are exposed to the EBC and TBC materials. While the primary concern of CMAS degradation is at temperatures above 1,200 °C, incongruent melting of CMAS may mean that reactions with EBC materials may occur at temperatures much lower than the full melting temperature. Future work will involve further characterization of the melt process to investigate composition evolution, including additional DSC scans to determine crystallization and melting kinetics. With decreasing $CaO:SiO_2$ ratio, the endpoint of melting for each composition shifted to higher temperatures, although this trend did not seem to influence the amount of amorphous content formed for each glass. At 1,200 °C, while results suggest near full crystallization of CMAS–1 and CMAS–3, both CMAS–2 and CMAS–2.5 contain substantial amounts of residual glass, as evidenced by the BSE micrographs (Figure 5(a) and Figure 6(d)). The greater presence of amorphous content in CMAS–2 and CMAS–2.5 at 1,200 °C could result in greater reactivity with these CMAS compositions at lower temperatures.

## 5.0 Conclusions

Four calcium-magnesium-aluminosilicate (CMAS) glass compositions were formulated from reference deposit chemistries and their melting and crystallization behaviors were evaluated. The variation of the $CaO:SiO_2$ ratio shifted the crystallization of the glasses into differing phase fields. Both CMAS–1 and CMAS–2 crystallize within the anorthite field of the quaternary, although CMAS–1 exhibited behavior consistent of a eutectic, whereas CMAS–2 exhibited incongruent melting behavior. Initial melting for both CMAS–1 and CMAS–2 occurred as low as ~1,050 °C, meaning that interactions with CMAS could occur lower than 1,200 °C. CMAS–2.5 and CMAS–3 both crystallize within $SiO_2$-regions of the quaternary, and like CMAS–2, exhibited incongruent melting behavior. Differential scanning calorimetry analyses suggest that the full melting temperatures of CMAS–2.5 and CMAS–3 are close to 1,500 °C, given that crystalline phases were still observed for these compositions at 1,400 °C. Although decreasing $CaO:SiO_2$ ratio raised the melting temperatures slightly, large residual amorphous content was still observed for CMAS–2 and CMAS–2.5 at 1,200 °C. Low-temperature interactions of the environmental barrier coating materials with these two compositions could be enhanced due to the greater availability of residual glass and melting of the glasses below their full melting temperatures.

## References


1. Padture, Nitin P.: Advanced Structural Ceramics in Aerospace Propulsion. Nat. Mater., vol. 15, 2016, pp. 804–809.
2. Lee, Kang N.: Environmental Barrier Coatings for $SiC_f$/SiC. Ceramic Matrix Composites: Materials, Modeling and Technology, Narottam P. Bansal and Jacques Lamon, eds., John Wiley & Sons, Inc., Hoboken, NJ, 2014, pp. 430–451.
3. Smialek, James L.: The Chemistry of Saudi Arabian Sand: A Deposition Problem on Helicopter Turbine Airfoils. NASA TM–105234, 1991. https://ntrs.nasa.gov

4. Borom, Marcus P.; Johnson, Curtis A.; and Peluso, Louis A.: Role of Environmental Deposits and Operating Surface Temperature in Spallation of Air Plasma Sprayed Thermal Barrier Coatings. Surf. Coat. Tech., vols. 86–87, no. 1, 1996, pp. 116–126.
5. Kim, J., et al.: Deposition of Volcanic Materials in the Hot Sections of Two Gas Turbine Engines. J. Eng. Gas Turbine Power, vol. 115, no. 3, 1993, pp. 641–651.
6. Song, Wenjia, et al.: Volcanic Ash Melting Under Conditions Relevant to Ash Turbine Interactions. Nat. Commun., vol. 7, no. 10795, 2016.
7. Song, Wenjia, et al.: Fusion Characteristics of Volcanic Ash Relevant to Aviation Hazards. Geophys. Res. Lett., vol. 41, no. 7, 2014, pp. 2326–2333.
8. Krämer, Stephen; Yang, James; and Levi, Carlos G.: Infiltration-Inhibiting Reaction of Gadolinium Zirconate Thermal Barrier Coatings With CMAS Melts. J. Am. Ceram. Soc., vol. 91, no. 2, 2008, pp. 576–583.
9. Poerschke, David L.; and Levi, Carlos G.: Effects of Cation Substitution and Temperature on the Interaction Between Thermal Barrier Oxides and Molten CMAS. J. Eur. Ceram. Soc., vol. 35, no. 2, 2015, pp. 681–691.
10. Ahlborg, Nadia L.; and Zhu, Dongming: Calcium–Magnesium Aluminosilicate (CMAS) Reactions and Degradation Mechanisms of Advanced Environmental Barrier Coatings. Surf. Coat. Technol., vol. 237, 2013, pp. 79–87.
11. Grant, Kendra M., et al.: Calcium–Magnesium Alumino-Silicate Interaction With Yttrium Monosilicate Environmental Barrier Coatings. J. Am. Ceram. Soc., vol. 93, no. 10, 2010, pp. 3504–3511.
12. Summers, William D., et al.: Roles of Composition and Temperature in Silicate Deposit-Induced Recession of Yttrium Disilicate. Acta Mater., vol. 160, 2018, pp. 34–46.
13. Wiesner, V.L.; Harder, Bryan J.; and Bansal, Narottam P.: High-Temperature Interactions of Desert Sand CMAS Glass With Yttrium Disilicate Environmental Barrier Coating Material. Ceram. Int., vol. 44, no. 18, 2018, pp. 22738–22743.
14. Stokes, Jamesa L., et al.: High-Temperature Thermochemical Interactions of Molten Silicates With $Yb_2Si_2O_7$ and $Y_2Si_2O_7$ Environmental Barrier Coating Materials. J. Eur. Ceram. Soc., vol. 39, no. 15, 2019, pp. 5059–5067.
15. Stokes, Jamesa L., et al.: Effects of Crystal Structure and Cation Size on Molten Silicate Reactivity With Environmental Barrier Coating Materials. J. Am. Ceram. Soc., vol. 103, no. 1, 2020, pp. 622–634.
16. Krämer, Stephan, et al.: Thermochemical Interaction of Thermal Barrier Coatings With Molten CaO-MgO-$Al_2O_3$-$SiO_2$ (CMAS) Deposits. J. Am. Ceram. Soc., vol. 89, no. 10, 2006, pp. 3167–3175.
17. Bansal, Narottam P.; and Choi, Sung R.: Properties of CMAS Glass From Desert Sand. Ceram. Int., vol. 41, no. 3, 2015, pp. 3901–3909.
18. Schroeder, Daniel V.: An Introduction to Thermal Physics. Addison Wesley, San Francisco, CA, 2000.
19. Peacor, Donald B.: High-Temperature Single-Crystal Study of the Cristobalite Inversion. Z. Kristallogr. Krist., vol. 138, 1973, pp. 274–298.
20. Mosesman, Max A.; and Pitzer, Kenneth S.: Thermodynamic Properties of the Crystalline Forms of Silica. J. Am. Chem. Soc., vol. 63, no. 9, 1941, pp. 2348–2356.
21. Heaney, Peter J.: Structure and Chemistry of the Low-Pressure Silica Polymorphs. Reviews in Mineralogy, P.J. Heaney, C.T. Prewitt, and G.V. Gibbs, eds., Vol. 29, Mineralogical Society of America, Chantilly, VA, 1994, pp. 1–40.

22. Mechnich, Peter; Braue, Wolfgang; and Schulz, Uwe: High-Temperature Corrosion of EB-PVD Yttria Partially Stabilized Zirconia Thermal Barrier Coatings With an Artificial Volcanic Ash Overlay. J. Am. Ceram. Soc., vol. 94, 2011, pp. 925–931.
23. Cai, C.Y., et al.: Microstructure Characteristics of EB-PVD YSZ Thermal Barrier Coatings Corroded by Molten Volcanic Ash. Surf. Coat. Technol., vol. 286, 2015, pp. 49–56.
24. Drexler, Julie M., et al.: Air-Plasma-Sprayed Thermal Barrier Coatings That Are Resistant to High-Temperature Attack by Glassy Deposits. Acta Mater., vol. 58, no. 20, 2010, pp. 6835–6844.
25. Perrudin, Francois, et al.: Gadolinium Oxide Solubility in Molten Silicate: Dissolution Mechanism and Stability of $Ca_2Gd_8(SiO_4)_6O_2$ and $Ca_3Gd_2(Si_3O_9)_2$ Silicate Phases. J. Eur. Ceram. Soc., vol. 37, 2017, pp. 2657–2665.
26. Yu, J., et al.: Hot Corrosion Behavior of $Y_4Al_2O_9$ Ceramics for Thermal Barrier Coatings Exposed to Calcium-Magnesium-Alumina-Silicate at 1250 °C. J. Eur. Ceram. Soc., vol. 39, 2019, pp. 1487–1495.
27. Aygun, Aysegul, et al.: Novel Thermal Barrier Coatings That Are Resistant to High-Temperature Attack by Glassy Deposits. Acta Mater., vol. 55, no. 20, 2007, pp. 6734–6745.
28. Goldsmith, Julian R.: The Melting and Breakdown Reactions of Anorthite at High Pressures and Temperatures. Am. Mineral., vol. 65, 1980, pp. 272–284.
29. Osborn, E.F., et al.: Optimum Composition of Blast Furnace Slag as Deduced From Liquidus Data for the Quaternary System CaO-MgO-$Al_2O_3$-$SiO_2$. JOM, vol. 6, 1954, pp. 33–45.